Density functional study of one- and two-component bottlebrush molecules in solvents of varying quality

Yuchong Zhang , Shun Xi , Arjun Valiya Parambathu & Walter G. Chapman

Published online: 23 May 2020.

Submit your article to this journal ☞

Article views: 60

View related articles ☞

View Crossmark data ☞

Taylor & Francis
Taylor & Francis Group

Check for updates

THERMODYNAMICS 2019 SPECIAL ISSUE

Density functional study of one- and two-component bottlebrush molecules in solvents of varying quality

Yuchong Zhang ⬤, Shun Xi, Arjun Valiya Parambathu and Walter G. Chapman

Department of Chemical and Biomolecular Engineering, Rice University, Houston, TX, USA

ABSTRACT
Modified inhomogeneous statistical associating fluid theory (iSAFT) density functional theory is extended to bottlebrush polymers in both good and poor solvent. The detailed structures of side chains in the implicit solvent are calculated and have a semi-quantitative agreement with simulation. The average brush heights calculated from the theory agree with well-established scaling theories. iSAFT is easily extended to model bottlebrush polymers with two or more components. For an amphiphilic core-shell bottlebrush polymer, if the solvent-phobic block is much shorter than the solvent-philic block, it will fold towards the backbone even though it resides at the free end of the side chain. Similarly, for an amphiphilic mixed-type bottlebrush polymer, the chain length of different components has a great impact on the structure and properties of the molecule. The molecule may not have the response (the switch of outer layer) towards the solvent treatment if one component is significantly longer than the other. Our results provide insight into the conformation of bottlebrush polymers as well as guidance in practical applications.
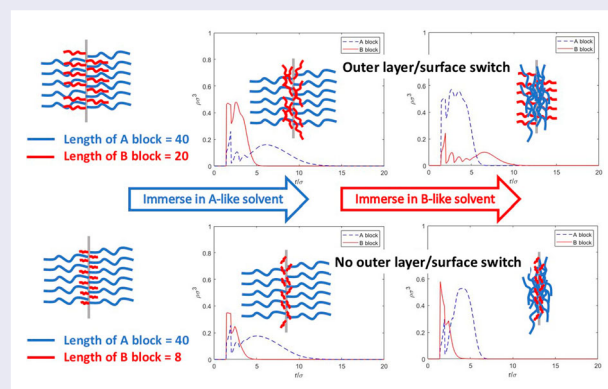
1. Introduction

Bottlebrush polymers contain polymeric side chains attached to a linear polymer backbone. Due to the tunable backbone length, side chain length, side chain composition and grafting density, properties of these polymers are highly designable. Applications of bottlebrush polymers are wide-ranging; these include photonic materials, lithographic patterning, drug delivery, and tumour detection and imaging [1].

There have been a few theoretical and simulation studies concerning the conformation of bottlebrush polymers [2–17]. Emphasis has been laid on both backbone and side chain conformations. Properties concerning backbones include but are not limited to contour length, persistence length and radius of gyration. For the side chain conformations, most interest has been shown in side chain layer thickness and radius of gyration. Backbone and side chains strongly influence each other [11,12,15,18]. For instance, as the grafting density of the side chains increases, the intrinsically flexible backbone is forced into an extended conformation. At the same time, the conformational changes of side chains due to varying solvent quality show different patterns if the backbone itself can extend or contract at various solvent strengths.

CONTACT Walter G. Chapman ✉ wgchap@rice.edu

Among all the models, it is interesting to consider a rigid backbone, which allows a thorough study of side chain conformations. Although somewhat simplified, the parameter space remains vast and makes the problem nothing near simple.

One pioneering work under this assumption is the work of Ball *et al.* [2]. They used self-consistent field theory to study the conformations of side chains in melt conditions and found that the end segments of side chains are excluded from a zone near the grafting surface. In contrast, Murat and Grest [9], who applied molecular dynamics simulation for a good solvent case, found no evidence for the existence of such a 'dead zone'. In the following year, Dan and Tirrell [19] utilised self-consistent field analysis and made an effort to resolve the discrepancies between the two previous works. They succeeded to some extent but also posted several new results. Later, Denesyuk [3] used a variational approach with a mean-field approximation to calculate the dominant trajectories of side chains, and found that the segment density in the centre of backbone was only slightly lower than that calculated near the backbone ends and local properties of bottlebrush polymers were fairly homogeneous. Sheiko *et al.* [13] identified different regions of conformations that side chains would fall in. At low grafting density, the side chains would not overlap with each other. So they behave like Gaussian coils in good solvent condition and individual globules in poor solvent condition. At higher grafting density, the side chains would interact with each other strongly. They became swollen brushes in good solvent and collapsed brushes or pearl-necklace clusters under poor solvent conditions. This classification of different states has been confirmed by the molecular dynamics simulations of Theodorakis *et al.* [14] and they further found that the transition between stretched and collapsed brushes occurred in a rather gradual manner.

Recently, researchers have paid more attention to the design and synthesis of bottlebrush polymers with side chains consisting of multiple components. As discussed in the review paper of Zhang and Müller [20], popular two-component bottlebrush polymers include block-type, mixed-type and core-shell-type. A block-type bottlebrush has side chains of the same component in a certain range of the backbone while a mixed-type bottlebrush has side chains of both components mixed along the backbone. Depending on the distribution of the two different side chains, their interaction parameters, and the nature of the solvent, side chains of a mixed-type bottlebrush can segregate into two different hemicylinders and these mixed-type bottlebrushes are also called Janus-type bottlebrushes. What block-type and mixed-type bottlebrush polymers have in common is that although there are two different components that form the side chains, within a single chain, there is only one component. By contrast, for the core-shell bottlebrush, each side chain is actually the same, but contains blocks of two components.

Due to the distinct properties of components and peculiar structure of the molecule, two-component bottlebrush polymers have diverse applications. In the study of Hong *et al.* [21], thin films were formed from the self-assembly of block-type bottlebrush polymers. Porous templates and scaffolds were further obtained by selective etching of one component. Mixed-type bottlebrush (no Janus structure forming) with hydrophobic polystyrene (PS) and hydrophilic poly(ethylene glycol) (PEG) side chains were synthesized by Li *et al.* [22] and displayed different surface properties in selective solvents, showing potential as stimuli-responsive coatings. Amphiphilic core-shell bottlebrush polymers may be potentially utilised as unimolecular micelles with advantages over the conventional micelles from linear amphiphilic diblock copolymers [23–25].

Again, with the assumption of a rigid backbone, several theoretical and simulation studies have been devoted to the study of side chain properties of two-component bottlebrush polymers. Theodorakis *et al.* [16] used Molecular Dynamics simulation to study the side chain conformations of a Janus-type bottlebrush polymer. They considered a symmetric binary system and found that chains of two different components collapsed independently at low grafting density but formed a Janus dumbbell-type structure at high grafting density. Erukhimovich *et al.* [4] studied the same type of system and further explored how solvent quality would affect the competition between the tendency of microphase separation to develop periodic order in the axial direction and the tendency to form a Janus-type structure. Polotsky *et al.* [10] used self-consistent field approach to study the structure of core-shell bottlebrush with a solvent-phobic inner block and a solvent-philic outer block. They found that a decrease in the solvent strength for the core block leads to an instability in the cylindrically uniform structure and the appearance of longitudinal undulations in the collapsed core, in agreement with their experimental observations.

In this work, we systematically study how different parameters will affect the side chain conformations using inhomogeneous statistical associating fluid theory (iSAFT). iSAFT is a density functional theory (DFT) for inhomogeneous complex polymeric fluids. Based on rigorous statistical mechanics [26–29], DFT is proved to provide detailed information for fluid structures at a calculation expense advantageous as compared to simulation methods. Compared with other theories such as self-consistent field theory, DFT can properly capture

local density fluctuations, such as 'layering' (density oscillations) near the wall. However, implementation of DFT formulation is usually non-trivial, especially in high dimensions or non-Cartesian coordinate systems. Reasonable assumptions and efficient algorithms are usually needed to facilitate computation. Following the work of Segura et al. [30], polyatomic DFTs were developed based on a bulk-free energy [31,32] for associating molecules or a free energy functional [33]. These DFTs demonstrated that the polyatomic system could be modelled as a mixture of associating atomic fluids in the limit of complete association. The free energy functional approach, called iSAFT, was extended to satisfy stoichiometry by Jain et al. [34] and further extended to study branched molecules [35] and associating polyatomic molecules [36], demonstrating the versatility to apply to molecules of different architecture. With appropriate adaptation, iSAFT has been successfully applied to investigate block copolymers in confinement [34], tethered polymers [37–40], polymer-colloid/nanoparticle mixtures [41–43], micelle formation [44,45] and dendrimer systems [46,47]. One can also turn to the paper by Emborsky et al. [48] for a good review.

To the best of our knowledge, no density functional approaches have been applied to the bottlebrush-type molecules. Thus, we extend iSAFT to study the conformations of side chains of a bottlebrush polymer in solvents of different quality. One advantage of DFT is that explicit solvent can be easily considered with little additional computational expense, but to provide consistency with other studies, solvent molecules are implicit in this study. The effect of solvent is incorporated in the interactions between polymer segments. We have also performed molecular dynamics simulations using LAMMPS to justify the iSAFT results. For clarity, simulation details are included in the appendix.

The paper is organised as follows. In Section 2, we explain the general iSAFT model. In Section 3, we model the side chains of a bottlebrush polymer in an implicit solvent and explore the effect of varying different parameters on chain conformations. Scaling analyses are performed for both good and poor solvent. We also extend the model to a core-shell bottlebrush polymer and a mixed-type bottlebrush polymer, studying how the molecular structure would be changed by varying the chain length of different components. The effect of explicit solvent will be the subject of another study. Section 4 gives our conclusion.

2. Model and theory

Our model is set up in cylindrical coordinates. We assume that the backbone is a rigid hard rod of infinite
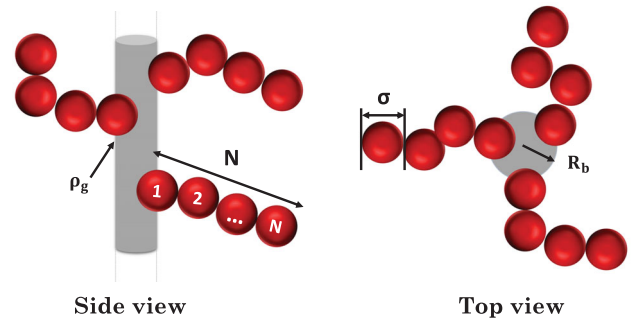

Figure 1. Schematic of bottlebrush polymer model.

length. The side chains are uniformly distributed on the surface of the backbone and each side chain is modelled as a flexible chain of tangentially bonded segments. The density of side chain segments is assumed to vary only along the direction perpendicular to the axis of the backbone, which is set as the origin. As depicted in Figure 1, structural parameters of this model include the grafting density of side chains ρ_g, length of side chains (or equivalently, number of side chain segments) N, radius of backbone R_b and diameter of segment σ, which is temperature-independent. The centre of the tethered segment is right at the backbone surface. All segments interact through repulsive and attractive contributions, given by the following pair potential:

$$u(r_{12}) = u^{\mathrm{ref}}(r_{12}) + u^{\mathrm{att}}(r_{12}) \tag{1}$$

where r_{12} is the distance between two segments.

The reference fluid contribution u^{ref} is taken as a hard sphere repulsive interaction

$$u^{\mathrm{ref}}(r_{12}) = u^{\mathrm{hs}}(r_{12}) = \begin{cases} \infty, & r_{12} < \sigma \\ 0, & r_{12} \geq \sigma \end{cases} \tag{2}$$

The intermolecular attractions u^{att} are described as a cut-shifted Lennard-Jones attraction with a Weeks, Chandler, and Andersen (WCA) separation [49,50]

$$u^{\mathrm{att}}(r_{12}) = \begin{cases} u^{\mathrm{LJ}}(r_{\min}) - u^{\mathrm{LJ}}(r_c) & \text{if } \sigma < r_{12} \leq r_{\min} \\ u^{\mathrm{LJ}}(r_{12}) - u^{\mathrm{LJ}}(r_c) & \text{if } r_{\min} < r_{12} \leq r_c \end{cases} \tag{3}$$

where

$$u^{\mathrm{LJ}}(r_{12}) = 4\epsilon^{\mathrm{LJ}} \left[\left(\frac{\sigma}{r_{12}} \right)^{12} - \left(\frac{\sigma}{r_{12}} \right)^{6} \right] \tag{4}$$

$r_{\min} = 2^{1/6}\sigma$ is the position of the Lennard-Jones potential minimum and $r_c = 3.5\sigma$ is the cut-off distance. The sum of u^{ref} and u^{att} serves as a good approximation of the cut-shifted Lennard-Jones potential as used in simulation (see Appendix for details).

2.1. iSAFT density functional theory

Traditional DFTs are formulated for an open system in the grand canonical ensemble. So the system is at fixed volume (V), temperature (T) and chemical potential (μ) in the presence of an external field ($V^{ext}(\mathbf{r})$). The grand free energy functional $\Omega[\rho]$ for a system of chain fluids can be related to the intrinsic Helmholtz free energy functional $A[\rho]$ as

$$\Omega[\rho_i(\mathbf{r})] = A[\rho_i(\mathbf{r})] - \sum_{i=1}^{N} \int d\mathbf{r}' \rho_i(\mathbf{r}')(\mu_i - V_i^{ext}(\mathbf{r}')) \tag{5}$$

where ρ_i is the density of segment i, μ_i is its chemical potential, V_i^{ext} is the external field acting on segment i, and the sum is over all the N segments of the chain. For the system at equilibrium, the grand free energy is minimised. Minimisation of the grand free energy with respect to the density of the segments yields a system of variational equations, known as the Euler–Lagrange equations

$$\frac{\delta A[\rho_i(\mathbf{r})]}{\delta \rho_i(\mathbf{r})} = \mu_i - V_i^{ext}(\mathbf{r}) \quad \forall\, i = 1, \ldots, N \tag{6}$$

The Helmholtz free energy functional can be decomposed into an ideal and excess contribution.

$$A[\rho_i(\mathbf{r})] = A^{id}[\rho_i(\mathbf{r})] + A^{ex,hs}[\rho_i(\mathbf{r})] + A^{ex,chain}[\rho_i(\mathbf{r})] + A^{ex,att}[\rho_i(\mathbf{r})] \tag{7}$$

The ideal contribution comes from the ideal gas state of the atomic mixture (id). The excess contribution of the free energy is due to excluded volume effects (hs), chain connectivity (chain) and long-range attraction (att).

The ideal gas functional is known exactly

$$\beta A^{id}[\rho_i(\mathbf{r})] = \int d\mathbf{r}_1 \sum_{i=1}^{N} \rho_i(\mathbf{r}_1)[\ln \rho_i(\mathbf{r}_1) - 1] \tag{8}$$

where $\beta = 1/(k_B T)$.

The hard sphere contribution $A^{ex,hs}[\rho_i(\mathbf{r})]$ is calculated from Rosenfeld's fundamental measure theory (FMT) [51] for a mixture of hard spheres

$$\beta A^{ex,hs}[\rho_i(\mathbf{r})] = \int d\mathbf{r}_1 \Phi[n_\alpha(\mathbf{r}_1)] \tag{9}$$

where $\Phi[n_\alpha(\mathbf{r})]$ is given by

$$\Phi[n_\alpha(\mathbf{r})] = -n_0 \ln(1 - n_3) + \frac{n_1 n_2 - \mathbf{n}_{v1} \cdot \mathbf{n}_{v2}}{1 - n_3}$$
$$+ \frac{n_2^3 - 3n_2(\mathbf{n}_{v2} \cdot \mathbf{n}_{v2})}{24\pi(1 - n_3)^2} \tag{10}$$

and $n_\alpha (\alpha = 0, 1, 2, 3, v1, v2)$ are the fundamental measures.

The attraction term $A^{ex,att}[\rho_i(\mathbf{r})]$ is accounted for by the mean-field approximation [52]

$$\beta A^{ex,att}[\rho_i(\mathbf{r})] = \frac{1}{2} \sum_{i=1}^{N} \sum_{j=1}^{N} \int d\mathbf{r}_1\, d\mathbf{r}_2 \beta u_{ij}^{att}(|\mathbf{r}_2 - \mathbf{r}_1|)$$
$$\times \rho_i(\mathbf{r}_1)\rho_j(\mathbf{r}_2) \tag{11}$$

Wertheim's TPT1 [26–29], as extended by Chapman [53], is used to calculate $A^{ex,chain}[\rho_i(\mathbf{r})]$ by forcing a mixture of spherical segments to bond in a specified order to form the chain. Thus, the chain contribution to the free energy functional is obtained by taking the complete bonding limit of an association free energy functional

$$\beta A^{ex,assoc}[\rho_i(\mathbf{r})] = \int d\mathbf{r}_1 \sum_{i=1}^{N} \rho_i(\mathbf{r}_1)$$
$$\times \sum_{\alpha \in \Gamma^{(i)}} \left(\ln \chi_\alpha^i(\mathbf{r}_1) - \frac{\chi_\alpha^i(\mathbf{r}_1)}{2} + \frac{1}{2} \right) \tag{12}$$

The first summation is over all segments i and the second is over all the association sites on segment i. χ_α^i denotes the fraction of segments of type i that are not bonded at their associating site α, which can be obtained by the law of mass action [30,53],

$$\chi_\alpha^i(\mathbf{r}_1) = \frac{1}{1 + \int d\mathbf{r}_2 \sum_{j=1}^{N} \rho_j(\mathbf{r}_2) \times \sum_{\beta \in \Gamma^{(j)}} \chi_\beta^j(\mathbf{r}_2)\Delta^{ij}(\mathbf{r}_1, \mathbf{r}_2)} \tag{13}$$

The association strength $\Delta^{ij}(\mathbf{r}_1, \mathbf{r}_2)$ is controlled by

$$\Delta^{ij}(\mathbf{r}_1, \mathbf{r}_2) = KF^{ij}(\mathbf{r}_1, \mathbf{r}_2)y^{ij}(\mathbf{r}_1, \mathbf{r}_2) \tag{14}$$

where K is a constant geometric factor which accounts for the entropic cost associated with the orientations and bonding volume of two segments. $F^{ij}(\mathbf{r}_1, \mathbf{r}_2)$ is the associating Mayer-f function given as [34]

$$F^{ij}(\mathbf{r}_1, \mathbf{r}_2) = \exp\left[\beta\epsilon_0 - \beta v_{bond}^{ij}(\mathbf{r}_1, \mathbf{r}_2)\right] - 1 \tag{15}$$

where ϵ_0 is the bond energy and $v_{bond}^{ij}(\mathbf{r}_1, \mathbf{r}_2)$ is the bonding potential. In the complete association limit of $\epsilon_0 \to \infty$, the chain contribution to the free energy $A^{ex,chain}[\rho_i(\mathbf{r})]$ can be obtained. For tangentially bonded segments, the bonding potential is given by

$$\exp\left[-\beta v_{bond}^{ij}(\mathbf{r}_1, \mathbf{r}_2)\right] = \frac{\delta(|\mathbf{r}_1 - \mathbf{r}_2| - \sigma^{ij})}{4\pi} \tag{16}$$

and $y^{ij}(\mathbf{r}_1, \mathbf{r}_2)$ is the cavity correlation function for inhomogeneous hard sphere reference fluid. $y^{ij}(\mathbf{r}_1, \mathbf{r}_2)$ is

approximated by [34]

$$\ln y^{ij}(\mathbf{r}_1, \mathbf{r}_2) = \frac{1}{2}\{\ln y^{ij}[\bar{\rho}_k(\mathbf{r}_1)] + \ln y^{ij}[\bar{\rho}_k(\mathbf{r}_2)]\} \quad (17)$$

where $\bar{\rho}_k(\mathbf{r}_1)$ is the weighted density of segment k at position $\mathbf{r}_1$. In the current work, a simple weighting is used

$$\bar{\rho}_k(\mathbf{r}_1) = \frac{3}{4\pi(\sigma_k)^3}\int_{|\mathbf{r}_1-\mathbf{r}_2|<\sigma_k} d\mathbf{r}_2\rho_k(\mathbf{r}_2) \quad (18)$$

and the expression for $y^{ij}[\bar{\rho}_k(\mathbf{r}_1)]$, the cavity correlation function for homogeneous hard sphere fluid, is only needed at contact and can be found at Equation (23) in the work of Tripathi and Chapman [33].

2.2. Functional derivatives of free energies

The functional derivatives of the free energies are given as

$$\frac{\delta\beta A^{\text{id}}[\rho_i(\mathbf{r})]}{\delta\rho_i(\mathbf{r})} = \ln\rho_i(\mathbf{r}) \quad (19)$$

$$\frac{\delta\beta A^{\text{ex,hs}}[\rho_i(\mathbf{r})]}{\delta\rho_i(\mathbf{r})} = \int d\mathbf{r}_1\frac{\delta\Phi[n_\alpha(\mathbf{r}_1)]}{\delta\rho_i(\mathbf{r})} \quad (20)$$

$$\frac{\delta\beta A^{\text{ex,att}}[\rho_i(\mathbf{r})]}{\delta\rho_i(\mathbf{r})} = \sum_{j=1}^{N}\int_{|\mathbf{r}-\mathbf{r}_1|>\sigma_{ij}} d\mathbf{r}_1\beta u_{ij}^{\text{att}}$$
$$\times (|\mathbf{r}-\mathbf{r}_1|)\rho_j(\mathbf{r}_1) \quad (21)$$

$$\frac{\delta\beta A^{\text{ex,chain}}[\rho_i(\mathbf{r})]}{\delta\rho_i(\mathbf{r})} = \sum_{\alpha\in\Gamma^{(i)}}\ln\chi_\alpha^i(\mathbf{r})$$
$$-\frac{1}{2}\sum_{j=1}^{N}\sum_{j'}^{\{j'\}}\int d\mathbf{r}_1\rho_j(\mathbf{r}_1)$$
$$\times\frac{\delta\ln y^{ij'}[\bar{\rho}_k(\mathbf{r}_1)]}{\delta\rho_i(\mathbf{r})} \quad (22)$$

where $\{j'\}$ is the set of all segments bonded to segment j. The first term on the right-hand side of Equation (22) enforces stoichiometry. The cavity correlation function is further approximated by its bulk counterpart evaluated at the weighted density as Equation (17).

Substituting the functional derivatives of the free energies in Euler–Lagrange equation Equation (6) gives

$$\ln\rho_i(\mathbf{r}) + \sum_{\alpha\in\Gamma^{(i)}}\ln\chi_\alpha^i(\mathbf{r}) = D_i(\mathbf{r}) + \beta(\mu_i - V_i^{\text{ext}}(\mathbf{r}))$$
$$(23)$$

where $D_i(\mathbf{r})$ is given by

$$D_i(\mathbf{r}) = -\frac{\delta\beta A^{\text{ex,hs}}[\rho_i(\mathbf{r})]}{\delta\rho_i(\mathbf{r})} - \frac{\delta\beta A^{\text{ex,att}}[\rho_i(\mathbf{r})]}{\delta\rho_i(\mathbf{r})}$$
$$+\frac{1}{2}\sum_{j=1}^{N}\sum_{j'}^{\{j'\}}\int d\mathbf{r}_1\rho_j(\mathbf{r}_1)\times\frac{\delta\ln y^{ij'}[\bar{\rho}_k(\mathbf{r}_1)]}{\delta\rho_i(\mathbf{r})}$$
$$(24)$$

2.3. Side chains tethered to the backbone

For the bottlebrush polymer model, we follow Figure 1 to denote segments. The external field exerted by the backbone surface on the tethered segment 1 is

$$V_1^{\text{ext}}(\mathbf{r}) = \begin{cases} u & \text{if } r = R_b \\ \infty & \text{otherwise} \end{cases} \quad (25)$$

and for other segments

$$V_i^{\text{ext}}(\mathbf{r}) = \begin{cases} \infty & \text{if } r < R_b + \sigma/2 \\ 0 & \text{otherwise} \end{cases} \quad (26)$$

The density of side chain segments can be expressed as follows. For segment 1,

$$\rho_1(\mathbf{r}_1) = \exp(\beta\mu_M - \beta u)\exp[D_1(\mathbf{r}_1)]$$
$$\times I_{1,1}(\mathbf{r}_1)I_{2,1}(\mathbf{r}_1)\delta(r_1 - R_b) \quad (27)$$

The delta function $\delta(r_1 - R_b)$ accounts for the fact that segment 1 is tethered at the backbone surface and for the other monomer segments $i = 2, \ldots, N$,

$$\rho_i(\mathbf{r}_i) = \exp(\beta\mu_M - \beta u)\exp[D_i(\mathbf{r}_i)]$$
$$\times I_{1,i}(\mathbf{r}_i)I_{2,i}(\mathbf{r}_i)\theta(r_i - R_b - \sigma/2) \quad (28)$$

where the Heaviside step function $\theta(r_i - R_b - \sigma/2)$ accounts for the fact that segments starting from $i = 2$ have to be at least $R_b + \sigma/2$ away from the axis. μ_M is the 'chemical potential' of the whole chain imposed by the tether condition. $I_{1,i}$ and $I_{2,i}$ are multiple integrals introduced by Jain et al. [34] to facilitate solving the Euler–Lagrange equations for linear chains. The integrals are solved using the following recurrence:

$$I_{1,1}(\mathbf{r}_1) = 1 \quad (29)$$

$$I_{1,i}(\mathbf{r}_i) = \int I_{1,i-1}(\mathbf{r}_{i-1})\exp[D_{i-1}(\mathbf{r}_{i-1})]$$
$$\times \Delta^{(i-1,i)}(\mathbf{r}_{i-1}, \mathbf{r}_i)d\mathbf{r}_{i-1} \quad (30)$$

and

$$I_{2,n}(\mathbf{r}_n) = 1 \tag{31}$$

$$I_{2,i}(\mathbf{r}_i) = \int I_{2,i+1}(\mathbf{r}_{i+1}) \exp[D_{i+1}(\mathbf{r}_{i+1})]$$
$$\times \Delta^{(i,i+1)}(\mathbf{r}_i, \mathbf{r}_{i+1}) \, d\mathbf{r}_{i+1} \tag{32}$$

The total density of side chain segments is calculated as

$$\rho_M(\mathbf{r}) = \sum_{i=1}^{N} \rho_i(\mathbf{r}) \tag{33}$$

The value of $\exp(\beta\mu_M - \beta u)$ can be obtained from the grafting density ρ_g as

$$\int \rho_1(\mathbf{r}_1) \, dr_1 = \exp(\beta\mu_M - \beta u) \exp[D_1(\mathbf{r}_1)]$$
$$\times I_{1,1}(\mathbf{r}_1) I_{2,1}(\mathbf{r}_1) = \rho_g \tag{34}$$

then we have

$$\exp(\beta\mu_M - \beta u) = \frac{\rho_g}{\exp[D_1(\mathbf{r}_1)] I_{1,1}(\mathbf{r}_1) I_{2,1}(\mathbf{r}_1)} \tag{35}$$

Substituting the equation into Equation (28) gives the density profile of all the other monomer segments. In this work, the radius of backbone R_b is set to be the same as σ, corresponding to a high curvature.

The density profile is solved using Picard's iteration method. The iterations start with a flat density profile as the initial guess and do not stop until the difference between two density profiles $\sum_{k=1}^{K} | \sum_{i=1}^{n} \rho_{i,k}^{new} - \sum_{i=1}^{n} \rho_{i,k}^{old}|$ is smaller than 10^{-5}. K is the maximum point of the discretisation mesh grid and n is the number of different segment types. Along with the assumption that there is only inhomogeneity along the radial direction, Fast Hankel Transformation Algorithm [54] is applied to facilitate the iterative evaluation of convolutions, with more details in the appendix.

3. Results and discussion

3.1. One-component bottlebrush polymer in implicit solvent

Before applying the theory to any case, it is important to check how good it is to assume that the density of side chain segments only varies along the direction perpendicular to the axis of the backbone. In Figure 2, we plot the density profiles along the axial direction from simulation for different combinations of N and ρ_g and for different solvent qualities. The athermal condition is equivalent to temperature being infinitely high, and thus representing a good solvent case. At $T^* = k_B T/\epsilon = 1$, where the side chain segments display strong attraction with each other,

represents a poor solvent case. Starting from a high grafting density $\rho_g = 0.5$, the density profiles are flat for both good and poor solvents despite the fluctuation from simulation, indicating conformations of swollen or collapsed brushes. At $\rho_g = 0.3$, the density profiles are overall flat for the good solvent case but show some sign of undulation for the poor solvent case, and the relative undulation is more obvious for a lower N. At $\rho_g = 0.1$, the undulation becomes significant even for the good solvent case and for the poor solvent case, we see that the sinusoid-like density profiles actually reach zero at certain positions for $N = 25, 50, 100$. This indicates the appearance of pinned or pearl-necklace clusters, in agreement with the studies of Sheiko et al. [13] and Theodorakis et al. [14]. Finally, at $\rho_g = 0.01$, for all chain length N considered, the density profiles in good or poor solvent show patterns of spikes, corresponding to the Gaussian coils or individual globules. In Figure 3, we show simulation snapshots of the five possible side chain conformations as described in the diagram of states by Sheiko et al. [13].

Therefore, the assumption that the density of side chain segments solely varies along the radial direction is only valid at relatively high grafting extent of side chains and this high grafting condition is even more stringent in the case of poor solvent. Similar observations have been made for a two-component mixed-type bottlebrush polymer by Erukhimovich et al. [4] using both weak segregation theory [55,56] and MD simulations. We also refer readers who are interested in axial/helical ordering to some other papers [10,57]. Consequently, to have convincing iSAFT results, we will limit our study to bottlebrush polymers of relatively high grafting extent (we do include several low grafting extent cases in the appendix and show the performances of our model under those conditions). For all the cases studied in the main contents, N and ρ_g are chosen that the grafting extent variable [13] $N^{1/2}\rho_g \geq 1.5$, which is the threshold obtained from the combination of $N = 25$ and $\rho_g = 0.3$.

We start with the effect of solvent quality on side chain conformations. We fix the segment number $N = 50$ and grafting density $\rho_g = 0.3$. As we can see from the Figure 4(a), the conformation of side chains transitions from a collapsed structure to a swollen structure as the temperature increases. There is good agreement between theory and simulation results. We see that iSAFT is also able to predict the oscillation behaviour of density profile near the backbone surface, with similar period and number of peaks as that of simulation. Another advantage of iSAFT is that densities of all individual segments are traceable. Figure 4(b) gives the density profiles of the end segments of side chains for different conditions. Besides the semi-quantitative agreement between theory and simulation, we also see that there are end segments in
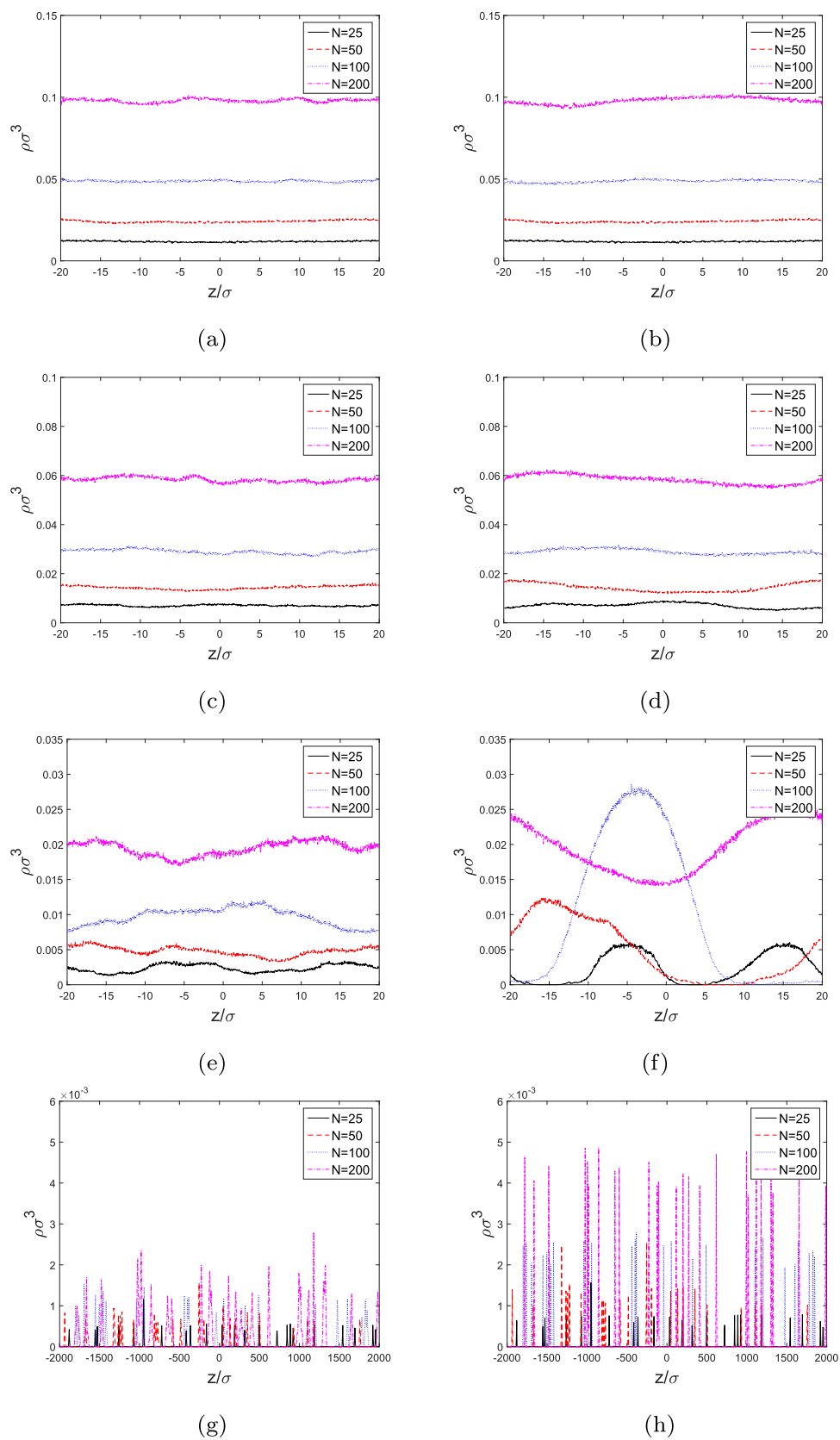
Figure 2. Axial density profiles of all segments for different conditions from MD simulation. (a) $\rho_g = 0.5$, athermal. (b) $\rho_g = 0.5$, $T^* = 1$. (c) $\rho_g = 0.3$, athermal. (d) $\rho_g = 0.3$, $T^* = 1$. (e) $\rho_g = 0.1$, athermal. (f) $\rho_g = 0.1$, $T^* = 1$. (g) $\rho_g = 0.01$, athermal. (h) $\rho_g = 0.01$, $T^* = 1$.
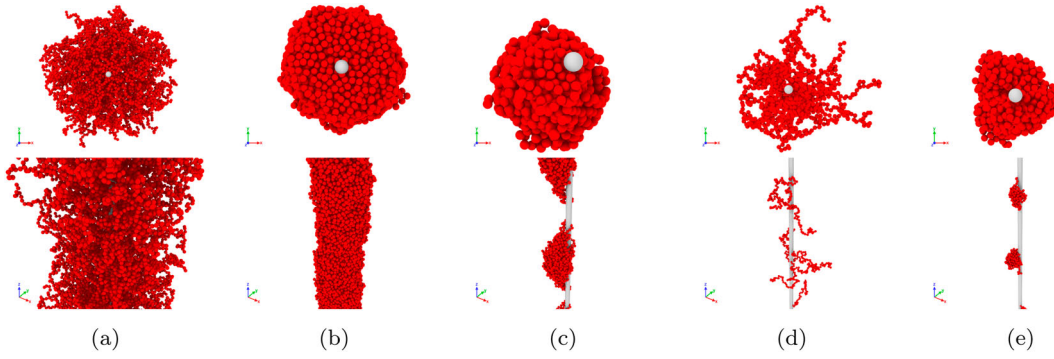
Figure 3. Simulation snapshots of five typical configurations. The upper row and the lower row show top views and side views, respectively. The diameter of all beads and the radius of the backbone are σ. Images are scaled for better visibility. $N = 50$ for all cases. (a) Swollen brushes at athermal condition and $\rho_g = 0.5$. (b) Collapsed brushes at $T^* = 1$ and $\rho_g = 0.5$. (c) Pinned clusters at $T^* = 1$ and $\rho_g = 0.1$. (d) Gaussian coils at athermal condition and $\rho_g = 0.01$. (e) Collapsed globules at $T^* = 1$ and $\rho_g = 0.01$.
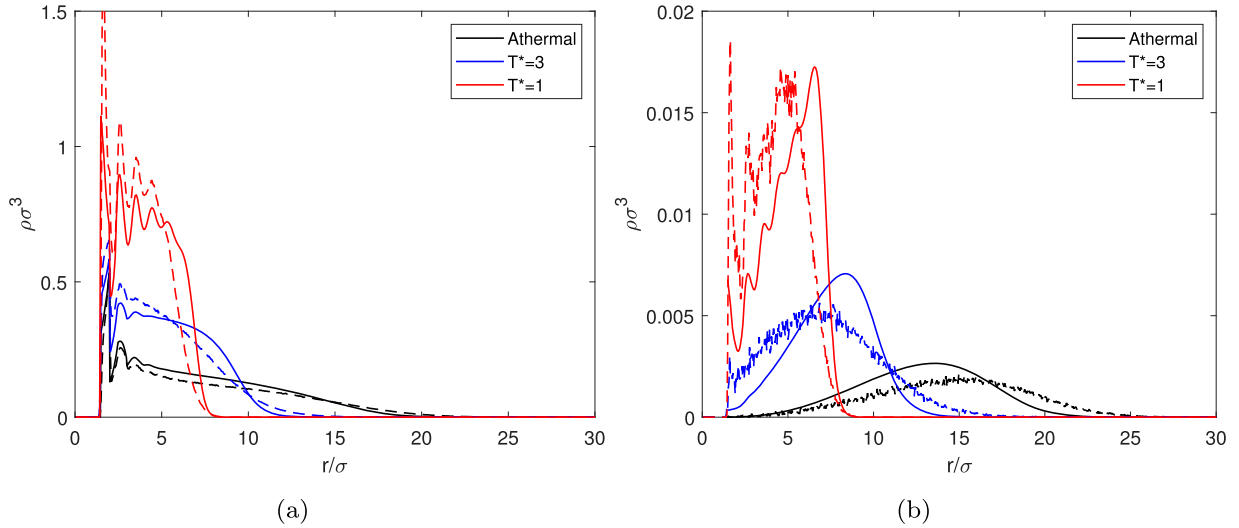

Figure 4. Radial density profiles of (a) all segments (b) end segment of side chains in solvents of varying quality. $\rho_g = 0.3, N = 50$. The solid lines represent iSAFT results and the dashed lines represent simulation results.

contact with the backbone and no 'dead zone' or 'exclusion zone' occurs. This is consistent with the finding of Murat and Grest [9].

We study the effect of side chain length N on the conformation of side chains. As shown in Figure 5, whether it is a good or poor solvent, an increase in side chain length will mainly result in a horizontal stretch of the density profile and the peak height is almost the same for the same solvent quality. However, we do see a lower peak height for the density profile of $N = 25$ at $T^* = 1$ compared to the others in Figure 5(b), more obviously from the simulation curve. The reason behind this result may be that the combination of $N = 25, \rho_g = 0.3$ has actually shifted from a high graft density region to an intermediate density region. The results in Figure 5 are also in qualitative agreement with results of scattering studies for bottlebrush sides chains. [18].

The effect of grafting density ρ_g on the conformation of side chains can be studied similarly. As shown in

Figure 6, with an increase of ρ_g, the density profile mainly heightens in the athermal case but widens at $T^* = 1$. This is because when the side chains are swollen in a good solvent, they are fully stretched and there is enough space to accommodate more chains. However, in a poor solvent, the sides chains are collapsed and densely packed near the backbone, and addition of new chains have to push segments further away from the backbone.

With the density profile, the average brush height of side chains (or layer thickness) $\langle h \rangle$ can be calculated from

$$\langle h \rangle = \frac{\int \rho(r)(r - R_b) 2\pi r \, dr}{\int \rho(r) 2\pi r \, dr} \quad (36)$$

Scaling theory predicts that the scaling variable for $\langle h \rangle$ changes with solvent quality. For sufficiently large grafting density, the average height $\langle h \rangle$ is dependent on both grafting density ρ_g and chain length N. It is predicted that for good solvent, $\langle h \rangle \sim N^{3/4} \rho_g^{1/4}$ and for poor solvent,
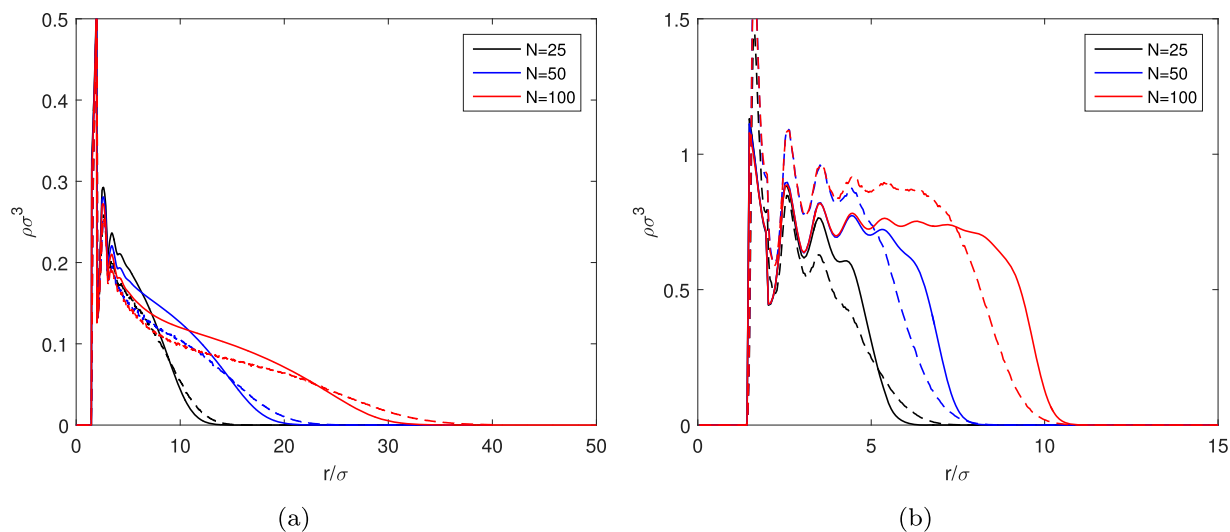
Figure 5. Radial density profiles of all segments for side chains of different length N at (a) athermal condition (b) $T^* = 1$. ρ_g is fixed at 0.3. The solid lines represent iSAFT results and the dashed lines represent simulation results.

Figure 6. Radial density profiles of all segments for side chains of different grafting density ρ_g at (a) athermal condition (b) $T^* = 1$. N is fixed at 50. The solid lines represent iSAFT results and the dashed lines represent simulation results.
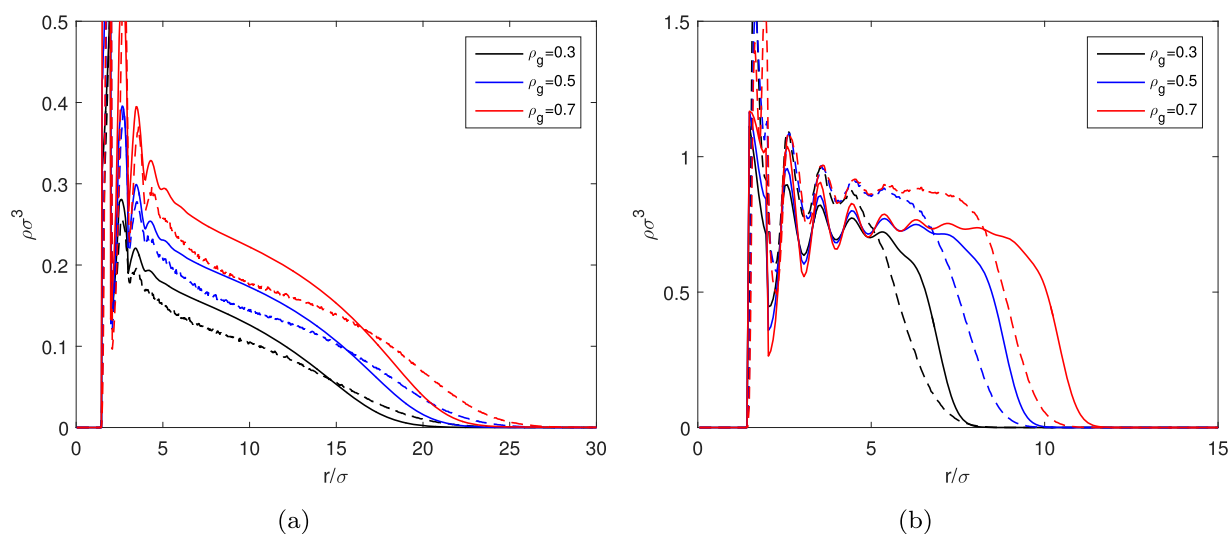
$\langle h \rangle \sim N^{1/2} \rho_g^{1/2}$ [13]. Figure 7 shows that iSAFT agrees with these scaling relations.

To conclude this section, we see that there is a semi-quantitative agreement between iSAFT and MD simulation for the results of one-component bottlebrush polymer. As mentioned in the introduction, iSAFT is computationally more efficient than MD simulations. From our computation, it takes on average around 10 min for iSAFT to get one density profile with only 1 processor. The computation time is mainly dependent on the granularity of discretisation (we set mesh grid number as 10^9 or 10^{10}) and the error tolerance allowed (10^{-5}). The computation is quite stable except for cases with a combination of high ρ_g and high N at the athermal condition. In a good solvent, the density profile of dense, long side chains tends to display a long flat tail with values close to zero, generating a region that is hard to converge. Using a finer discretisation mitigates the issue, while the algorithm itself needs to be improved for better robustness. In comparison, it takes from 2 min to 2 h for MD simulation to get results of one case, with 24 processors. The computation time of MD simulation varies a lot and is highly dependent on the number of beads. (See implementation details in the appendix.)

The accuracy of the iSAFT density functional theory is remarkable given the simplicity of the theory. As discussed above, the solution algorithm that assumes inhomogeneity in only the radial direction introduces some error in the DFT, particularly at low grafting density. Differences between iSAFT and simulation results also
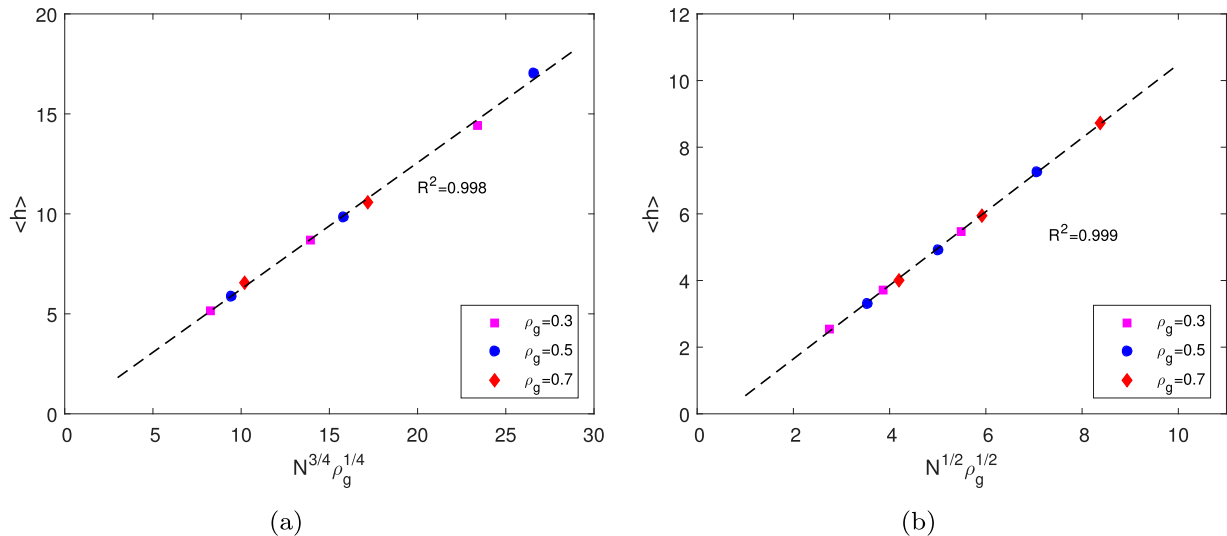
Figure 7. (a) Average Brush height $\langle h \rangle$ vs $N^{3/4}\rho_g^{1/4}$ at athermal condition for combinations of $\rho_g = 0.3, 0.5, 0.7$ and different side chain length. (b) Average Brush height $\langle h \rangle$ vs $N^{1/2}\rho_g^{1/2}$ at $T^* = 1$ for combinations of $\rho_g = 0.3, 0.5, 0.7$ and different side chain length. Symbols of different shapes are theoretical results at different ρ_g. Dashed curves are linear fits to the data.

arise from inaccuracies in the contributions to the free energy functional and due to approximations in the solution approach. For example, long-range attractions are estimated as a mean-field attraction in this work, meaning that only first-order corrections are included and the pair correlation function is set equal to one. A weighted density approximation of $A^{ex,att}[\rho_i(\mathbf{r})]$ has been shown to give better results in some cases [58,59]. However, we believe that the primary reason for any discrepancy between theory and simulation is due to approximations in the chain free energy functional. iSAFT is based on extensions of thermodynamic perturbation theory of first-order (TPT1), so the chain free energy functional includes only two body correlations and neglects chain–chain correlations (the single chain approximation) [60]. Thus improved agreement between simulation and theory will result from the incorporation of multibody correlations, particularly intramolecular correlations, in the chain free energy functional and along the bottlebrush. Recent studies that incorporate multibody correlations and include chain–chain correlations for bulk fluids show the potential of extending iSAFT [60–62].

3.2. Two-component bottlebrush polymer in implicit solvent

It is easy to extend iSAFT to study the two-component bottlebrush polymer, especially in the case of core-shell type bottlebrush polymer since it will usually only have one-dimensional density variance, which is along the radial direction. While the block-type bottlebrush polymer obviously displays inhomogeneity along the axial direction, the mixed-type bottlebrush polymer might also show only radial density variance if the two types of segments are quite dissimilar in response to the solvent and no Janus structure forms. In this section, we will use iSAFT to model both core-shell-type and mixed-type bottlebrush polymers.

As for the two types of segments, we denote them as A and B, and set the interaction energy between segments as $\epsilon_{AA}^* = 0.8, \epsilon_{BB}^* = 0.2$ and $\epsilon_{AB}^* = 0$. $\epsilon^* = \epsilon/(k_B T)$ is the reduced energy parameter. This parameterization mimics the case that segment A is solvent-phobic, segment B is solvent-philic, A and B interact as hard chains towards each other.

3.2.1. Core-shell bottlebrush polymer

For core-shell bottlebrush polymers, we firstly model the case where block A is tethered to the backbone. We fix the number of A segments $N_A = 25$ and vary the number of B segments N_B. As we see in Figure 8, the segments of A block are compressed near the backbone surface and we see an extended conformation of block B starting from where A segments vanish. As we vary N_B, there is hardly any change in the conformation of block A but a more stretched structure for block B due to the increase of chain length. It indicates that A segments will simply hide inside the bottlebrush polymer, shielded by the outer layer of B segments.

Then, we switch the roles of block A and B, tethering block B to the backbone. Similarly, we fix the number of B segments $N_B = 25$ and vary the number of A segments N_A. When $N_A = 5$, we see that A block
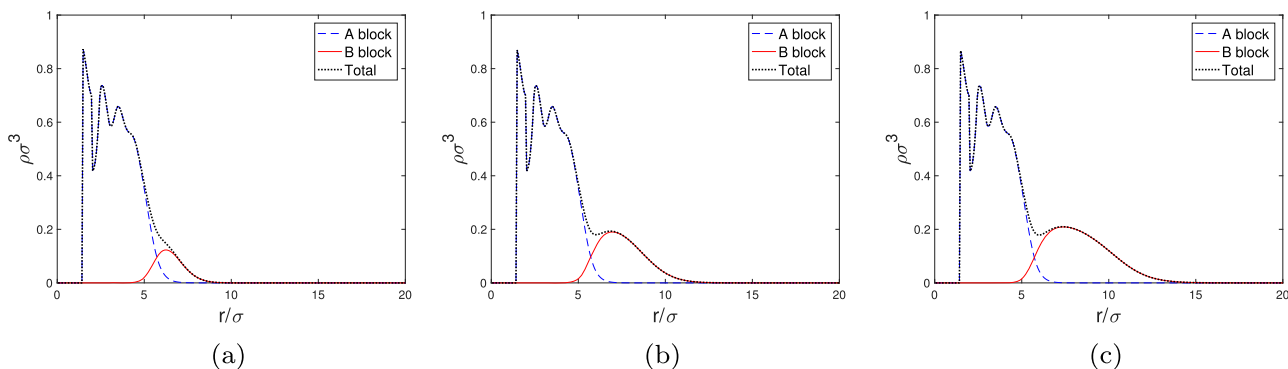
Figure 8. Radial density profiles of segments A and B and total (dashed, solid and dotted lines) when block A is tethered to the backbone. Number of segment A, N_A is fixed at 25 and number of segment B, N_B is 5 in (a), 15 in (b) and 25 in (c). Other parameters: $\rho_g = 0.3$, $\epsilon^*_{AA} = 0.8$, $\epsilon^*_{BB} = 0.2$, $\epsilon^*_{AB} = 0$.

folds back towards the backbone surface and it is partly shielded by B block. As N_A increases, A block starts to migrate to the exterior of bottlebrush polymer, forming a more and more compressed layer. Although there are still a few B segments around, we see an overwhelming dominance of A segments at the outer layer. These different conformations of side chains are illustrated in Figure 9. In this system, A block is solvent-phobic and would rather stay near the backbone to hide from the solvent, while B block likes contact with the solvent. This is the enthalpic effect. On the other hand, folding back of A block creates a region with high density and limits the mobility of B block, resulting in a larger entropic penalty. The different structures presented in Figure 9 are a result of the competition between the enthalpic effect and entropic cost, aiming to reach minimum free energy.

3.2.2. Mixed-type bottlebrush polymer

For mixed-type bottlebrush polymers, we set that both A side chains and B side chains have a grafting density $\rho_g = 0.15$. For $N_A = N_B = 40$, from Figure 10(c), we see that the side chains form a bi-layer structure and B segments dominate the outer layer. If another solvent is used and makes the effect that $\epsilon^*_{AA} = 0.2$ and $\epsilon^*_{BB} = 0.8$, we would expect the switch of two layers and reversibility of surface properties. The PS-PEG mixed-type bottlebrush polymer synthesized by Li *et al.* [22] showed an increase in water contact angle after treatment with cyclohexane vapour and a decrease after treatment with methanol vapour. They also found that the length of side chains played a role in determining contact angle and compositional changes. Therefore, similar to the study of core-shell bottlebrush polymers, we vary N_A and N_B to see how the structure changes accordingly. As shown in Figure 10, for all cases considered, A segments and B segments separate into two layers. The outer layer is made up of B segments except for the case of $N_A = 40$ and

$N_B = 8$. In Figure 10(e), side chain B collapses although it is solvent-philic. The mechanism behind this effect is still the competition of enthalpic and entropic effects. While side chain A wants to reduce the unfavourable contact with side chain B and solvents, the short side chain B cannot afford too strong entropic stretching. As a result, the free energy is minimised with both side chains collapsing and A segments dominating the outer layer.

If we look at Figure 10(b,d) together, it works just like we change the quality of the solvent and thus switch the chemical affinity of two types of segments with the solvent. In both cases, the outer layer is formed by chains consisting of the solvent-philic segments regardless of the chain length. However, comparing Figure 10(a,e) together, we find that it is the longer chains forming the outer layers regardless of the solvents being favourable or unfavourable towards them. This indicates that if the side chain of one component is significantly longer than the other, the molecule may not have the response (outer layer switch) towards the solvent treatment. This finding is in line with the water contact angle measurements of PS-PEG mixed-type bottlebrush polymer [22]. The PS6K-m-PEG5K bottlebrush polymer has a contact angle of 72.5° if treated by cyclohexane vapour and 63.8° if treated by methanol vapour. By contrast, the contact angle of PS6K-m-PEG2K drops from 74.8° with cyclohexane treatment to 71.1° with methanol treatment. Besides the difference in flexibility of PS and PEG chains, the chain length disparity may account for the relative smaller change of contact angle for PS6K-m-PEG2K, which implies a less sensitive solvent response.

The results in this section show that if we want to study the surface properties of a core-shell or mixed-type bottlebrush polymer, it is important to know the compositions of the outer layer, and that can be highly dependent on the design of side chains. Given the comparable size of monomers and flexibility of chains, chain (or block)
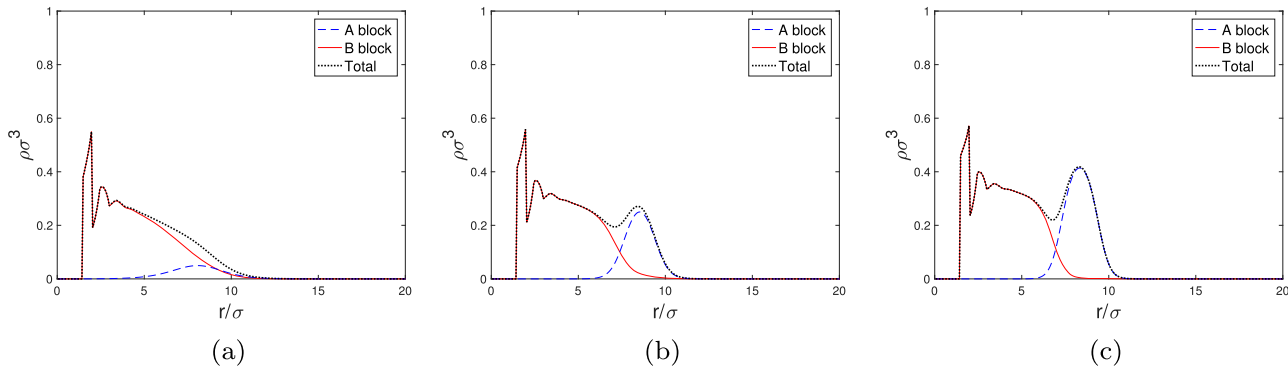
Figure 9. Radial density profiles of segments A and B and total (dashed, solid and dotted lines) when block B is tethered to the backbone. Number of segment B, N_B is fixed at 25 and number of segment A, N_A is 5 in (a), 15 in (b) and 25 in (c). Other parameters: $\rho_g = 0.3$, $\epsilon_{AA}^* = 0.8$, $\epsilon_{BB}^* = 0.2$, $\epsilon_{AB}^* = 0$.
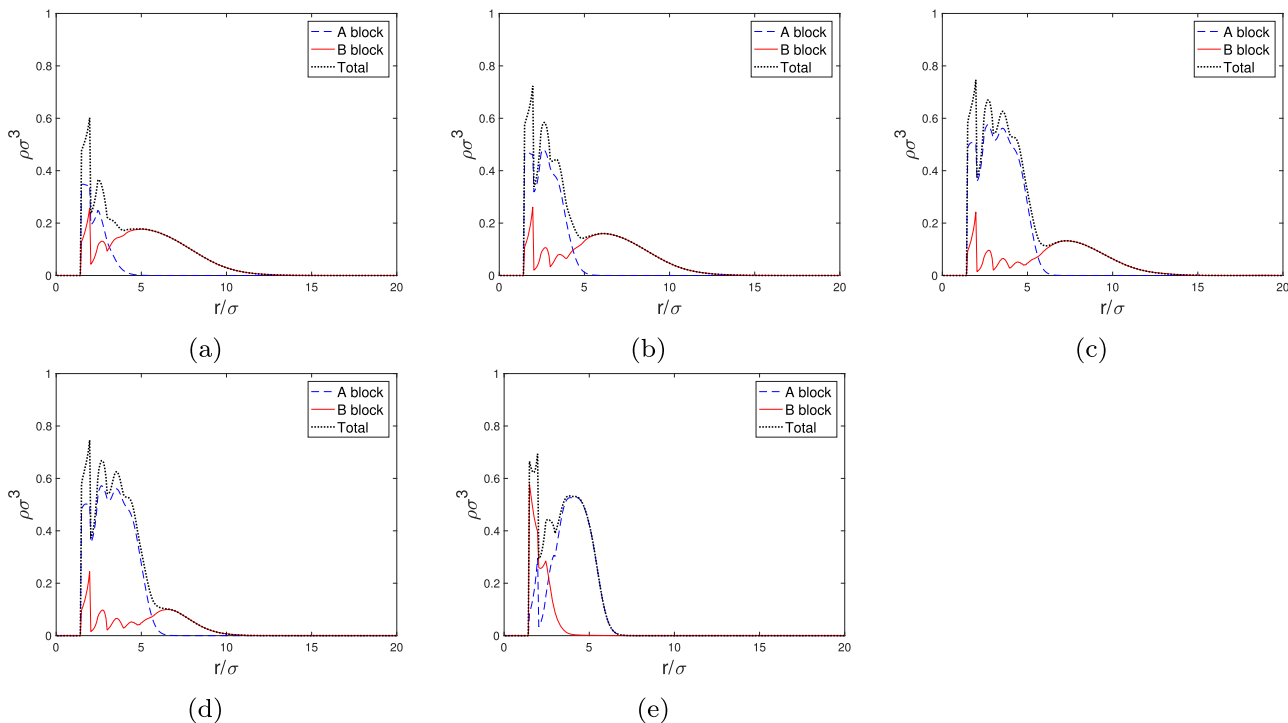

Figure 10. Radial density profiles of segments A, B and total (dashed, solid and dotted lines) for a mixed-type bottlebrush polymer. (a) $N_A = 8, N_B = 40$. (b) $N_A = 20, N_B = 40$. (c) $N_A = 40, N_B = 40$. (d) $N_A = 40, N_B = 20$. (e) $N_A = 40, N_B = 8$. Other parameters: $\rho_g = 0.15$ for both chain A and chain B, $\epsilon_{AA}^* = 0.8$, $\epsilon_{BB}^* = 0.2$, $\epsilon_{AB}^* = 0$.

length of different components can be a key factor. In the future, we will consider the explicit solvent, which not only makes a more realistic system, but also introduces other important factors such as solvent size.

4. Conclusion

We have applied iSAFT to study the structure of side chains of a bottlebrush polymer at high grafting extent. An implicit solvent is considered. Although a rigid bottlebrush backbone is assumed, we have found a variety of polymer conformations for different solvent qualities. In addition, no 'dead zone' is discovered for the conditions studied. By changing the grafting density or side chain length, the radial density profile will shift following certain patterns. The theoretical results reach a semi-quantitative agreement with our molecular dynamics simulation. The scaling relationship for the brush height is consistent with previous literature. The one-component model is further extended to a two-component model and we explore the surface properties of a core-shell or mixed-type bottlebrush polymer consisting of amphiphilic components. The theory predicts

that the composition of the outer layer is dependent on the chain (block) length of two components. This type of knowledge is important in the design and application of responsive materials. Compared with molecular simulation, iSAFT has the great advantage of computational efficiency and the future work will focus on inclusion of explicit solvent and extension of iSAFT to a 2D space, potentially relaxing constraints such as infinite length of backbone, and providing more insights into real applications.

Acknowledgments

Disclosure statement

No potential conflict of interest was reported by the author(s).

Funding

ORCID

Yuchong Zhang 🆔 http://orcid.org/0000-0002-6809-1020

References

[1] R. Verduzco, X. Li, S.L. Pesek and G.E. Stein, Chem. Soc. Rev. **44** (8), 2405–2420 (2015).
[2] R. Ball, J. Marko, S. Milner and T. Witten, Macromolecules **24** (3), 693–703 (1991).
[3] N. Denesyuk, Phys. Rev. E **68** (3), 031803 (2003).
[4] I. Erukhimovich, P.E. Theodorakis, W. Paul and K. Binder, J. Chem. Phys. **134** (5), 054906 (2011).
[5] H.-P. Hsu, W. Paul and K. Binder, Macromol. Theory. Simul.**16** (7), 660–689 (2007).
[6] H.-P. Hsu, W. Paul, S. Rathgeber and K. Binder, Macromolecules **43** (3), 1592–1601 (2010).
[7] H. Li and T.A. Witten, Macromolecules **27** (2), 449–457 (1994).
[8] X. Ma, Y. Yang, L. Zhu, B. Zhao, P. Tang and F. Qiu, Chemical Physics J. Chem. Phys. **139** (21), 214902 (2013).
[9] M. Murat and G.S. Grest, Macromolecules **24** (3), 704–708 (1991).
[10] A. Polotsky, M. Charlaganov, Y. Xu, F.A. Leermakers, M. Daoud, A.H. Muller, T. Dotera and O. Borisov, Macromolecules **41** (11), 4020–4028 (2008).
[11] S. Rathgeber, T. Pakula, A. Wilk, K. Matyjaszewski, H.-i. Lee and K.L. Beers, Polymer **47** (20), 7318–7327 (2006).
[12] M. Saariaho, I. Szleifer, O. Ikkala and G. Ten Brinke, Theory and Simulations Macromol. Theory. Simul. **7** (2), 211–216 (1998).
[13] S. Sheiko, O. Borisov, S. Prokhorova and M. Möller, Euro. Phys. J. E **13** (2), 125–131 (2004).
[14] P. Theodorakis, W. Paul and K. Binder, EPL (Euro. Lett.) **88** (6), 63002 (2009).
[15] P.E. Theodorakis, H. -P. Hsu, W. Paul and K. Binder, Chemical Physics J. Chem. Phys. **135** (16), 164903 (2011).
[16] P.E. Theodorakis, W. Paul and K. Binder, Macromolecules **43** (11), 5137–5148 (2010).
[17] A. Yethiraj, Chemical Physics J. Chem. Phys. **125** (20), 204901 (2006).
[18] B. Zhang, F. Gröhn, J.S. Pedersen, K. Fischer and M. Schmidt, Macromolecules **39** (24), 8440–8450 (2006).
[19] N. Dan and M. Tirrell, Macromolecules **25** (11), 2890–2895 (1992).
[20] M. Zhang and A.H. Müller, J. Polymer Sci. Part A: Polymer Chem. **43** (16), 3461–3481 (2005).
[21] S.W. Hong, W. Gu, J. Huh, B.R. Sveinbjornsson, G. Jeong, R.H. Grubbs and T.P. Russell, Nano ACS Nano. **7** (11), 9684–9692 (2013).
[22] X. Li, S.L. Prukop, S.L. Biswal and R. Verduzco, Macromolecules **45** (17), 7118–7127 (2012).
[23] R. Djalali, N. Hugenberg, K. Fischer and M. Schmidt, Rapid Communications Macromol. Rapid. Commun. **20** (8), 444–449 (1999).
[24] V. Heroguez, Y. Gnanou and M. Fontanille, Macromolecules **30** (17), 4791–4798 (1997).
[25] H. Tang, Y. Li, S.H. Lahasky, S.S. Sheiko and D. Zhang, Macromolecules **44** (6), 1491–1499 (2011).
[26] M. Wertheim, Statistical Physics J. Stat. Phys. **35** (1), 19–34 (1984).
[27] M. Wertheim, Statistical Physics J. Stat. Phys. **35** (1–2), 35–47 (1984).
[28] M. Wertheim, Statistical Physics J. Stat. Phys. **42** (3), 459–476 (1986).
[29] M. Wertheim, Statistical Physics J. Stat. Phys. **42** (3), 477–492 (1986).
[30] C.J. Segura, W.G. Chapman and K.P. Shukla, Mol. Phys. **90** (5), 759–772 (1997).
[31] Y.-X. Yu and J. Wu, Chemical Physics J. Chem. Phys. **117** (5), 2368–2376 (2002a).
[32] Y.-X. Yu and J. Wu, Chemical Physics J. Chem. Phys. **116** (16), 7094–7103 (2002b).
[33] S. Tripathi and W.G. Chapman, Chemical Physics J. Chem. Phys.**122** (9), 094506 (2005).
[34] S. Jain, A. Dominik and W.G. Chapman, Chemical Physics J. Chem. Phys. **127** (24), 244904 (2007).
[35] S. Jain, Unpublished doctoral dissertation. Rice University. 2009.
[36] A. Bymaster and W.G. Chapman, J. Phys. Chem. B **114** (38), 12298–12307 (2010).
[37] K. Gong and W.G. Chapman, Chemical Physics J. Chem. Phys. **135** (21), 214901 (2011).
[38] K. Gong, B.D. Marshall and W.G. Chapman, Chemical Physics J. Chem. Phys. **137** (15), 154904 (2012).
[39] K. Gong, B.D. Marshall and W.G. Chapman, Chemical Physics J. Chem. Phys. **139** (9), 094904 (2013).
[40] S. Jain, P. Jog, J. Weinhold, R. Srivastava and W.G. Chapman, Chemical Physics J. Chem. Phys. **128** (15), 154910 (2008).
[41] A. Bymaster, S. Jain and W.G. Chapman, Chemical Physics J. Chem. Phys. **128** (16), 164910 (2008).
[42] A.L. Frischknecht, V. Padmanabhan and M.E. Mackay, Chemical Physics J. Chem. Phys. **136** (16), 164904 (2012).
[43] E. McGarrity, A. Frischknecht, L. Frink and M. Mackay, Review Letters Phys. Rev. Lett. **99** (23), 238302 (2007).

[44] L. Wang, A. Haghmoradi, J. Liu, S. Xi, G.J. Hirasaki, C.A. Miller and W.G. Chapman, J. Chem. Phys. **146** (12), 124705 (2017).
[45] S. Xi, L. Wang, J. Liu and W.G. Chapman, Langmuir (2019).
[46] Y. Zhang and W.G. Chapman, Langmuir **35** (33), 10808–10817 (2019).
[47] Y. Zhang, A. Valiya Parambathu and W.G. Chapman, Chemical Physics J. Chem. Phys. **149** (6), 064904 (2018).
[48] C.P. Emborsky, Z. Feng, K.R. Cox and W.G. Chapman, Fluid. Phase. Equilib.**306** (1), 15–30 (2011).
[49] D. Chandler and J.D. Weeks, Review Letters Phys. Rev. Lett. **25** (3), 149 (1970).
[50] J.D. Weeks, D. Chandler and H.C. Andersen, C Physics J. Chem. Phys. **54** (12), 5237–5247 (1971).
[51] Y. Rosenfeld, Review Letters Phys. Rev. Lett. **63** (9), 980 (1989).
[52] J.-P. Hansen and I.R. McDonald, *Theory of Simple Liquids* (Elsevier, 1990).
[53] W.G. Chapman, PhD thesis. Cornell University. 1988.
[54] S. Xi, J. Liu, A. Valiya Parambathu, Y. Zhang and W.G. Chapman, Indust. Engin. Chem. Res. (2020).
[55] L. Leibler, Macromolecules **13** (6), 1602–1617 (1980).
[56] I.Y. Yerukhimovich, Polymer Sci. USSR **24** (9), 2223–2232 (1982).
[57] I. Erukhimovich and A. Johner, EPL (Euro. Lett.) **79** (5), 56004 (2007).
[58] M. Heier, S. Stephan, J. Liu, W.G. Chapman, H. Hasse and K. Langenbach, Mol. Phys. **116** (15–16), 2083–2094 (2018).
[59] E. Sauer and J. Gross, Ind. Eng. Chem. Res. **56** (14), 4119–4135 (2017).
[60] B.D. Marshall and W.G. Chapman, Adv. Chem. Phys. 1 (2016).
[61] A. Bansal, D. Asthagiri, K.R. Cox and W.G. Chapman, Chemical Physics J. Chem. Phys. **145** (7), 074904 (2016).
[62] Y. Zhang and W.G. Chapman, Ind. Eng. Chem. Res. **57** (5), 1679–1688 (2018).
[63] S. Plimpton, J. Comput. Phys. **117** (1), 1–19 (1995).
[64] Sandia National Laboratories. Lammps (2018). http://lammps.sandia.gov.
[65] A. Stukowski, Model. Simulat. Mater. Sci. Engin. **18** (1), 015012 (2009).
[66] M.P. Sears and L.J. Frink, J. Comput. Phys. **190** (1), 184–200 (2003).

Appendices

Appendix 1. Simulation details

Molecular dynamics simulations were used to simulate a single bottlebrush polymer in implicit solvent. The molecule was modelled as a rod grafted with polymeric side chains at the given density. The side chains are made of bead-spring freely jointed united-atom monomers. The non-bonded interactions and the monomer–rod interactions are calculated with a truncated and shifted Lennard-Jones potential. The 12-6 Lennard-Jones potential form is used.

$$u^{LJ}(r) = 4\epsilon^{LJ}\left[\left(\frac{\sigma}{r}\right)^{12} - \left(\frac{\sigma}{r}\right)^{6}\right] \tag{A1}$$

where ϵ^{LJ} is the well depth, σ is the particle diameter and r is the distance. The potential reaches its minimum at $r_{min} = 2^{1/6}\sigma$.

The monomer–monomer interactions are given as

$$u_{ss}(r_{ij}) = u^{LJ}(r_{ij}) - u^{LJ}(r_c) \tag{A2}$$

where r_{ij} is the distance between the centres of the two beads. For all monomers, mass $m = 1, \epsilon^{LJ} = 1, \sigma = 1$, and $r_c = 3.5\sigma$. For athermal case, we changed the cut-off radius to $r_c = r_{min}$.

The monomer–rod interactions is given as

$$u_{rs}(r_{iz}) = u^{LJ}(r_{iz} - R_b + 0.5\sigma) - u^{LJ}(r_{min}) \tag{A3}$$

where r_{iz} is the distance of the centre of the bead from the axis of the rod. R_b is the radius of the rod or backbone. It should be noted that the grafted bead remains fixed, and does not interact with the rod.

The bonded monomer interactions is represented by a harmonic potential.

$$u^{bond}(r_{ij}) = K(r_{ij} - r_0)^2 \tag{A4}$$

where $K = 1662\epsilon^{LJ}/\sigma^2$ is the spring constant and $r_0 = \sigma$ is the equilibrium bond length.

The initial configuration was constructed as follows. The grafting monomers were randomly placed on the surface of the rod at the given density. The side chains were then grown radially outwards to the given chain length. The simulations were carried using LAMMPS molecular dynamics code [63,64]. All the snapshots were generated using The Open Visualisation Tool (OVITO) [65]. The rod axis was aligned in the z-direction with the centre at the origin of the xy plane, and periodic boundary conditions were established. The system size in the xy dimensions were adjusted ensuring there is minimum of 20σ space between the molecule and its periodic image, avoiding any interactions between them. The height of the rod was set at 40σ. The time step was chosen as $\Delta t = 0.0012\tau$, where $\tau = \sigma\sqrt{m/\epsilon^{LJ}}$. The temperature T^* was controlled using Nosé–Hoover thermostat with a damping factor of 3τ. All simulations were minimised using conjugate gradient method and initialised at a temperature of $T^* = 6.5$. The system was then cooled to the desired temperature in 5×10^5 time steps, and further relaxed at the given temperature for 5×10^5 time steps. The thermostat was then turned off and a production run was carried out for 1×10^6 steps, saving frames every 1000 time steps.

Appendix 2. Fast Hankel Transform Algorithm

In this appendix, we outline the steps to evaluate the weighted densities which are the convolutions

$$n_i^\alpha(\mathbf{r}) = \int \rho_i(\mathbf{r}')\omega^\alpha(R_i - |\mathbf{r} - \mathbf{r}'|)\,\mathrm{d}\mathbf{r}' \tag{A5}$$

According to the convolution theorem, the Fourier transformed convolution $n_i^\alpha(\mathbf{r})$ can be expressed as

$$\tilde{n}_i^\alpha(\mathbf{k}) = \tilde{\rho}_i(\mathbf{k})\tilde{\omega}^\alpha(\mathbf{k}) \tag{A6}$$

where $\tilde{\rho}_i(\mathbf{k})$ and $\tilde{\omega}^\alpha(\mathbf{k})$ are the Fourier transformed density distribution and weighting functions. The basic strategy to evaluate the convolutions in modified iSAFT is to first evaluate the Fourier transforms of the convolution then perform an inverse transform to the transformed convolutions.

Following this route, free energy functional derivatives from different contributions can be numerically evaluated by Fourier transform. The transforms of fundamental measure theory free energy functional derivatives are given by Sears and Frink [66]. The Fourier transform of mean-field contribution can be expressed as

$$\frac{\delta \tilde{A}^{att}}{\delta \tilde{\rho}_i(\mathbf{k})} = \sum_j \tilde{\rho}_i(\mathbf{k}) \beta \tilde{u}_{ij}(\mathbf{k}) \qquad (A7)$$

where $\beta \tilde{u}_{ij}(\mathbf{k})$ is the Fourier transform of WCA perturbation attractive potential mentioned before.

There are two contributions to the chain connectivity in modified iSAFT. One is the direct chain term $\delta A^{chain,dir}/\delta\rho_i(\mathbf{r}) = -\frac{1}{2}\sum_{j=1}^{N}\sum_{j'}^{\{j'\}} \int d\mathbf{r}' \rho_j(\mathbf{r}')(\delta \ln y^{jj'}/\delta\rho_i(\mathbf{r}))$. This direction

chain term has a Fourier transform

$$\frac{\delta \tilde{A}^{chain,dir}}{\delta \tilde{\rho}_i(\mathbf{k})} = -\frac{1}{2}\sum_{j=1}^{N}\sum_{j'}^{\{j'\}} \tilde{\rho}_j(\mathbf{k}') \frac{\partial \ln \tilde{y}^{jj'}}{\partial \tilde{\bar{\rho}}_i(\mathbf{k})} \frac{\delta \tilde{\bar{\rho}}_i}{\delta \tilde{\rho}_i(\mathbf{k})} \qquad (A8)$$

where the Fourier transform of the weighting function for chain term $\frac{\delta \tilde{\bar{\rho}}_i}{\delta \tilde{\rho}_i(\mathbf{k})}$ has an analytic form

$$\frac{\delta \tilde{\bar{\rho}}_i}{\delta \tilde{\rho}_i(\mathbf{k})} = \frac{3[\sin(2|\mathbf{k}|R_i) - 2|\mathbf{k}|R_i \cos(2|\mathbf{k}|R_i)]}{(2|\mathbf{k}|R_i)^3} \qquad (A9)$$

and the Fourier transform of partial derivative of cavity correlation function with respect to weighted density $\tilde{\rho}_j(\mathbf{k}')(\partial \ln \tilde{y}^{jj'}/\partial \tilde{\bar{\rho}}_i(\mathbf{k}))$ has to be numerically evaluated.

The second contribution to chain connectivity in modified iSAFT is the recursive integral $I_{1,i}(\mathbf{r}_i)$ and $I_{2,i}(\mathbf{r}_i)$ as stated
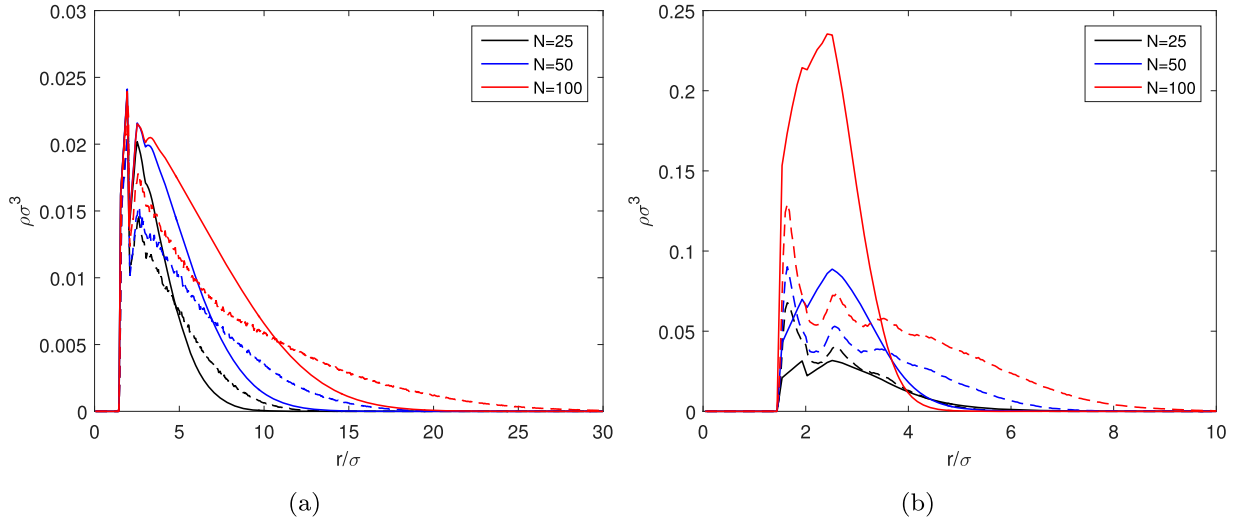

Figure A1. Radial density profiles of all segments for side chains of different length N at (a) athermal condition (b) $T^* = 1$. ρ_g is fixed at 0.01. The solid lines represent iSAFT results and the dashed lines represent simulation results.
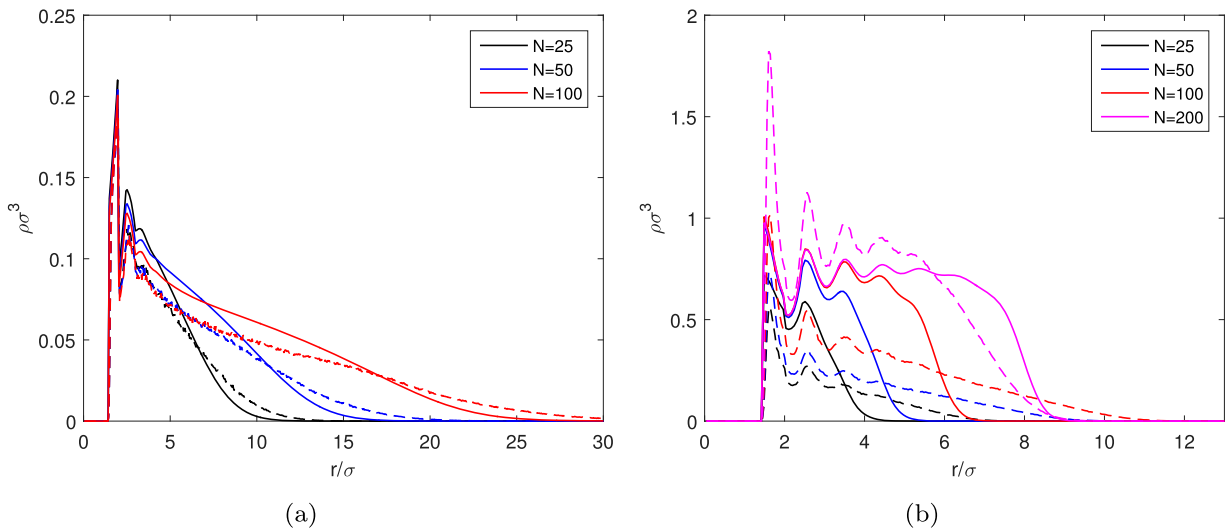

Figure A2. Radial density profiles of all segments for side chains of different length N at (a) athermal condition (b) $T^* = 1$. ρ_g is fixed at 0.1. The solid lines represent iSAFT results and the dashed lines represent simulation results.
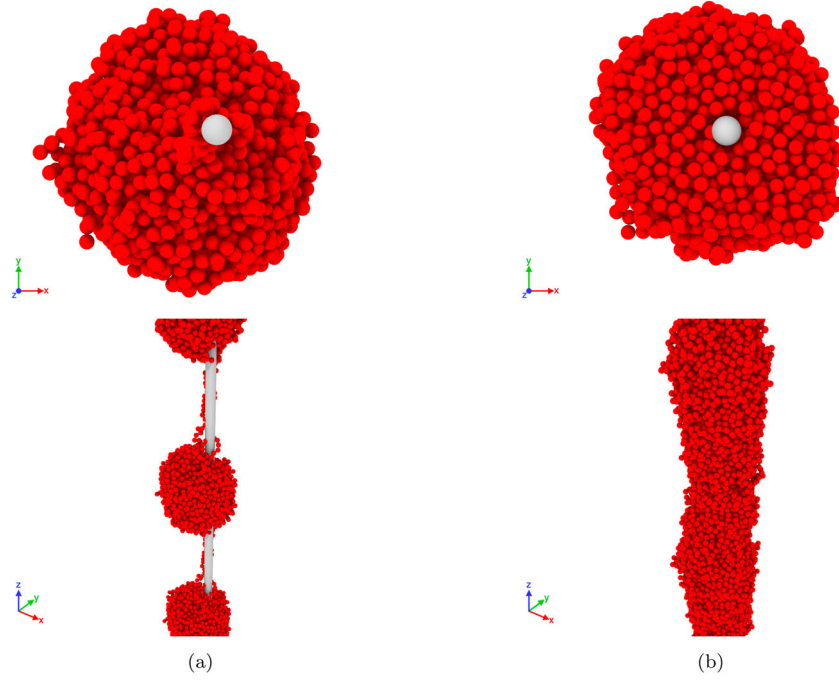
Figure A3. Simulation snapshots at $\rho_g = 0.1$ and $T^* = 1$. The upper row and the lower row show top views and side views, respectively. The diameter of all beads and the radius of the backbone are σ. Images are scaled for better visibility. (a) $N = 100$. (b) $N = 200$.

previously. The Fourier transforms of those recursive integrals are $\tilde{I}_{1,i}(\mathbf{k}_i)$ and $\tilde{I}_{2,i}(\mathbf{k}_i)$. They are also evaluated in a recursive fashion in Fourier space

$$\tilde{I}_{1,i}(\mathbf{k}_i) = \mathcal{F}\left\{\frac{\delta(|\mathbf{r}_j - \mathbf{r}_{j-1}| - \sigma_{j-1,j})}{4\pi\sigma_{j-1,j}^2}\right\}$$
$$\times \mathcal{F}\{I_{1,i}(\mathbf{r}_i)\exp[D_{j-1}(\mathbf{r}_{j-1})]\} \qquad (A10)$$

where the first part is body-averaged weighting function and it has an analytic form

$$\mathcal{F}\left\{\frac{\delta(|\mathbf{r}_j - \mathbf{r}_{j-1}| - \sigma_{j-1,j})}{4\pi\sigma_{j-1,j}^2}\right\} = \frac{\sin(|k|\sigma_{j-1,j})}{|k|\sigma_{j-1,j}} \qquad (A11)$$

The Fourier transform of the second part has to be numerically evaluated.

Appendix 3. iSAFT model for low grafting conditions

As we discussed, the assumption that there is only inhomogeneity along the radial direction for the density of side chain segments is no longer valid at low grafting extent. When the grafting density is low enough, the side chains barely overlap. They behave as Gaussian coils in a good solvent and as collapsed globules in a poor solvent. Even for a moderate grafting density, the side chains may form pinned clusters in a poor solvent.

Here, we present several low-density cases where the single dimension of inhomogeneity approximation is 'mistakenly' applied and see how the results could deviate from simulation results. In Figure A1, we see there is significant disagreement between iSAFT and simulation results at $\rho_g = 0.01$ for all values of N considered, particularly in the poor solvent case. In Figure A2, $\rho_g = 0.1$ and we see a good agreement for the good solvent case. This is consistent with Figure 2(e), where there is some but not severe fluctuation in density along the axial direction. For the poor solvent case, iSAFT with the single dimension of inhomogeneity cannot capture the simulation results except for the case of $N = 200$, where the simulation curve is apparently different from those of lower N. Again, in Figure 2(f), we see the three curves corresponding to $N = 25$, 50 and 100 reach zero at several positions while the density profile for $N = 200$ have substantial values at all positions despite the oscillatory behaviour. In Figure A3, we take simulation snapshots of bottlebrush polymers at $\rho_g = 0.1$ and $T^* = 1$ for $N = 100$ and $N = 200$, respectively. It clearly shows that the side chains form pinned clusters for $N = 100$ but become collapsed brushes for $N = 200$.

All these results further verify that with the single inhomogeneity assumption, iSAFT is only able to handle relatively high grafting bottlebrush polymers, or more specifically, conformations of swollen or collapsed brushes. In addition, both ρ_g and N play a role in determining the grafting extent of the side chains.